

OVERVIEW AND ACTUAL UNDERSTANDING OF THE ELECTRON CLOUD EFFECT AND INSTABILITIES IN THE FUTURE LINEAR COLLIDERS*

M. T. F. Pivi[†], SLAC, Stanford University, Menlo Park, California 94025, USA

Abstract

The electron cloud is potentially an important effect in linear colliders. Many of the effects have been evaluated. Actions to suppress the electron cloud are required for the GLC/NLC positron main damping ring (MDR or DR) and the low emittance transport lines as well as for the TESLA damping ring. There is an ongoing R&D program studying a number of possible remedies to reduce the secondary electron yield below that required. For more detailed information and development, refer to the paper by M. Pivi and K. Ohmi [1], following the proceedings of the ECLOUD04 workshop.

INTRODUCTION

The electron cloud effects are known limitations in storage rings with positively charged particles such as protons or positrons [2]. The electron cloud was identified as a possible limitation in the damping rings of a future linear collider in the ILC TRC document [3]. Extensive studies on the possible electron cloud effect have been performed at SLAC for the GLC/NLC, also referred as X-Band, and the TESLA positron main damping rings (MDR) [4, 5, 6] as well as the positron Low Emittance Transport which includes the bunch compressor system (BCS), the main linac, and the beam delivery system (BDS). The results are obtained by computer simulation codes [7, 8, 9, 10, 11] developed to study the electron cloud effect in particle accelerators. Electron cloud studies for TESLA as well as for CLIC are also discussed in [12, 13].

Our studies usually proceed in two steps: first, the effects of the electron cloud on the beam are studied to determine limits on the allowable cloud density and, second, the cloud generation is studied to determine the level of remediation required. If the cloud is not suppressed, it will grow until it reaches an equilibrium density close to neutralization, ratio e/p , but in most cases the interaction of the cloud with the positron beam sets a much lower limit on the acceptable cloud density. The electron cloud can have three primary effects on the positron beams. It can cause coupled bunch instabilities, coherent single bunch instabilities, or incoherent tune spreads that lead to increased vertical emittance much as the space charge tune spread can lead to beam size increases. In general, the electron cloud effects in the linear colliders are so severe that the generation of

a cloud in a significant fraction of the rings or beam lines will have deleterious effects. We have estimated the equilibrium density level as well as the threshold for the single-bunch instability in both linear collider damping rings and the coupled-bunch instability in the X-band main damping ring. For example, we have estimated the electron cloud density threshold for the single-bunch fast head-tail instability in the X-band and TESLA damping rings. The results have been benchmarked with three different simulation codes, namely HEAD-TAIL [8], QUICKPIC [10] and PEHTS [11].

LINEAR COLLIDERS DESIGN

Damping Rings

Damping rings are necessary to reduce the emittances produced by the particle sources to the small values required for the linear collider. A summary of the main parameters of the damping ring is given in Table 1. A conceptual layout of the TESLA positron damping ring [5] is shown in Fig. 1, with the long straight section, injection/ejection sections, wigglers, and RF placed in the main linac tunnel. The TESLA main damping ring stores 2820 bunches with a 20 ns bunch spacing. The bunch spacing in the TESLA DR design is compressed to reduce the length of the DR. In particular, the rise and fall time of the injection/extraction kicker ≤ 20 ns determine the bunch spacing and the 17 km length of the TESLA damping ring. Research is underway to develop a faster kicker that may allow reducing the length of the damping ring. The vacuum chamber in the long TESLA straight sections is a round aluminum pipe with a radius 50 mm, while in the arcs and wiggler sections it is reduced in size. The actual design does not include an antechamber in the arcs.

The NLC damping ring complex is shown in Fig. 2. The NLC and GLC Damping Rings are very similar in concept and parameters.

The NLC positron MDR stores 3 trains, separated by 65 ns with each train consisting of 192 bunches having a 1.4 ns bunch spacing. The aluminum vacuum chamber is round with a radius 20 mm and includes an antechamber to remove most of the synchrotron radiation.

Low Emittance Transport Lines

The bunches are extracted individually from the TESLA DR. In the low emittance transport lines from the damping ring to the interaction point (IP), the bunch spacing is 337 ns or 176 ns, respectively, in the 500 GeV or 800 GeV

*Work supported by the US DOE under contracts DE-AC03-76SF00515 and DE-AC03-76SF00098.

[†]mpivi@slac.stanford.edu

Table 1: Simulation parameters for the GLC/NLC or X-band and the TESLA positron Damping Rings.

Parameter	Symbol, unit	X-Band	TESLA
Ring circumference	C , m	299.8	17000
Bunch population	N_p , 10^{10}	0.75	2
Number of train/bunches		3×192	1×2820
Circulating current	I_b , mA	690	160
Bunch length	σ_z , mm	5.5	6.0
Bunch size in arc sections	σ_x, σ_y μm	49, 6	103, 7
Bunch size in wiggler	σ_x, σ_y μm	"	93, 5
Bunch size in long straight sections	σ_x, σ_y μm	-	345, 345
Arc chamber semi-axes	a, b , cm	2, 2	2.2, 1.8
Long (TESLA) straights chamber semi-axes	a, b , cm	-	5, 5
Beta functions at kick sections	β_x, β_y m	2.2, 4.6	35, 65.7
Long. mom. spread	$\Delta p/p$	9.7×10^{-4}	1.3×10^{-3}
Mom. compaction	α	1.33×10^{-3}	1.22×10^{-4}
Synchrotron tune	ν_z	0.0118	6.59×10^{-2}
Horizontal tune	ν_x	21.150	76.31
Vertical tune	ν_y	10.347	41.18
Chromaticity	ξ_x, ξ_y	correct.	correct.
Arc dipole			
Dipole field	B , T	0.675	0.194
Dipole length	l , m	2.0	9
Horizontal bend angle	$\Delta\theta$, rad	0.2	0.1047
Critical photon energy	E_c , keV	1.7	3.2
Radiation power per horizontal mrad	W/mrad	15	16
Damping Wigglers			
Strength wiggler K-value	K	54	59.7
Magnetic field gap center	B_0 , T	2.1	1.6
Wiggler sections in ring		2	2
Wiggler section length	L_w , m	30	250
Wiggler period	λ_w , m	0.27	0.4
Chamber semi-axes	a, b , mm	8, 8	16, 9

c.m. configurations. The number of bunches per train is 2820 with a repetition rate of 5 Hz. In the X-Band low emittance transport lines from the damping ring to the interaction point (IP), the bunch spacing is maintained 1.4 ns with bunch trains consisting of 192 bunches and a repetition rate 120 Hz. Synchrotron radiation analytic estimates for the damping rings and simulations for the low emittance transport lines of both linear collider designs, are presented in [14] and for the TESLA design also in [13].

GENERATION OF THE ELECTRON CLOUD MODEL DESCRIPTION

Parameters determining the cloud formation are the secondary electron yield (SEY), which is the number of secondary electrons generated per incident electron, and the energy spectrum of the secondary emitted electrons. The SEY $\delta(E_0)$ and the corresponding emitted-electron energy spectrum $d\delta/dE$ (E_0 =incident electron energy, E =emitted secondary energy) are represented by a de-

tailed model described elsewhere [17]. The electron reflectivity at low electron energy is assumed $\sim 50\%$, or $\delta(0) = 0.5$, when the peak SEY value is $\delta_{\max} = 2.0$. In the SEY model, the energy value E_{\max} at which the SEY peaks, is assumed to vary with δ_{\max} [18] due to conditioning. Typically, $E_{\max} = 240$ eV at $\delta_{\max} = 1.7$ and $E_{\max} = 170$ eV at $\delta_{\max} = 1.1$. The electron cloud develops under conditions where the average SEY of the electrons hitting the beam pipe wall is larger than one, and increases until an equilibrium electron density level is reached.

SYNCHROTRON RADIATION IN THE DAMPING RINGS

TESLA DR Arc Dipole Magnet

The cold option damping ring (at the moment of printing this paper, the cold option is based on the TESLA design) is designed to operate at a beam energy 5 GeV [5]. The arc lattice is designed as a minimum emittance cell with

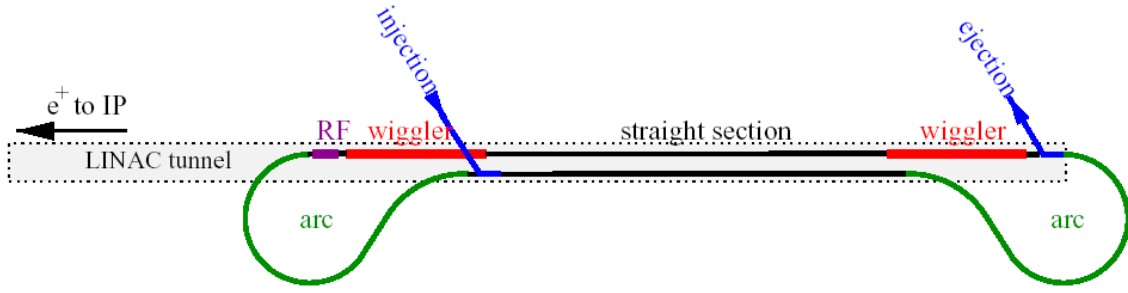


Figure 1: TESLA Damping ring conceptual layout.

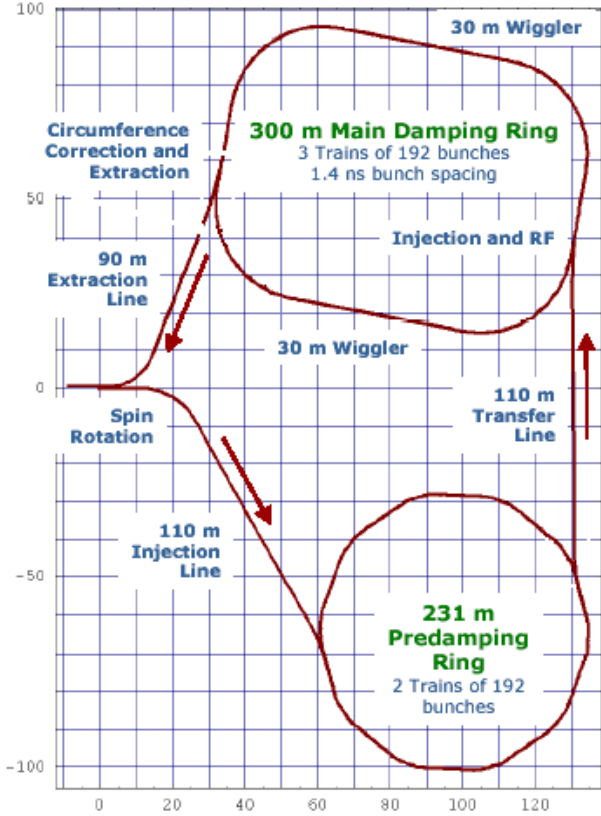


Figure 2: NLC positron DR complex layout. The NLC and GLC Damping Rings are very similar in concept and parameters.

a 6° dipole flanked by quadrupole doublets. The resulting cell length is 15.2 m and the dipoles are made long 9 m to increase the momentum compaction factor. The bending radius is 85.9 m, thus the bend angle is $\varphi_B = 0.1$ rad. At the moment, the TESLA design does not include an antechamber. Electron cloud studies, see also below, suggest that an antechamber design should be provided to remove most of the synchrotron radiation from the arc chambers.

We estimate analytically [14, 15, 16] the number of photons intercepted by the antechamber and the photons emitted at sufficiently large angles to hit the vacuum chamber

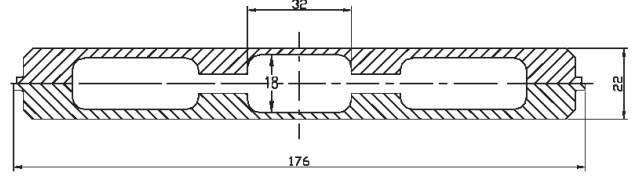


Figure 3: TESLA Damping ring wiggler vacuum chamber.

wall.

The total number of photons radiated in the bend per beam particle per radian is given by the well known formula

$$N_{\gamma, \text{tot}} = \frac{5\alpha\gamma}{2\sqrt{3}} \Delta\theta \quad (1)$$

where $\Delta\theta$ is the angle subtended by the magnet ($\alpha \simeq 1/137$ is here the fine structure constant). The total number of photons emitted per bend is given by $N_{\gamma, \text{tot}} \simeq 10.7$ with $\Delta\theta = 0.2$ rad. The angular photon flux N_γ is given by

$$\frac{d^2 N_\gamma}{d\omega d\Omega} = \frac{3\alpha\gamma^2\omega}{4\pi^2} \left(\frac{1}{\omega_c}\right)^2 (1 + \gamma^2\theta_y^2)^2 \times \left[K_{2/3}^2(\xi) + \frac{\gamma^2\theta_y^2}{1 + \gamma^2\theta_y^2} K_{1/3}^2(\xi) \right] \quad (2)$$

where ω_c is the critical photon frequency, θ_y is the angle of observation in the vertical plane, $d\Omega$ the solid emission angle, r_e is the classical electron radius, γ is the Lorentz factor, K_x are the modified Bessel functions of the second kind, and the parameter ξ is

$$\xi = \frac{\omega}{2\omega_c} (1 + \gamma^2\theta_y^2)^{3/2}. \quad (3)$$

We now consider an antechamber design and define the minimum vertical emission angle θ_{\min} for the photon to hit the chamber. Integrating Eq. (2) over the frequency spectrum and over the vertical angle one obtains the number of photons hitting the inside of the vacuum chamber per radian and beam particle

$$N_\gamma(\theta_{\min}) = 2 \int_{\omega_m}^{\infty} d\omega \int_{\theta_{\min}}^{\pi/2} d\theta_y \frac{d^2 N_\gamma}{d\omega d\Omega} \quad (4)$$

where ω_m is the minimum photon frequency. The result of the integration is shown in Fig. 4 where photons of all

energies and photons with energy $W > \hbar\omega_m = 4$ eV are considered in the calculations. In this latter case we have

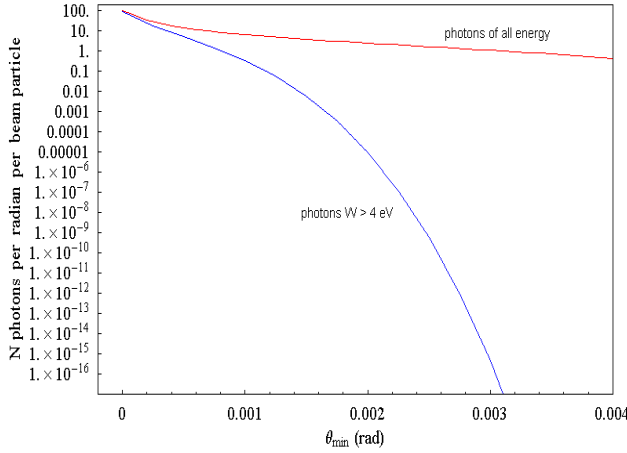


Figure 4: Number of photons of all energies and with an energy > 4 eV hitting the vacuum chamber per beam particle and per radian as a function of the emission angle θ_{\min} .

assumed that the minimum photon energy needed for photoelectron emission is 4 eV. Since the minimum emission angle is a function of the emission location inside the bend, $\theta_{\min} = \theta_{\min}(\varphi)$, the number of photons hitting the chamber is given by

$$N_{\gamma, \text{mag}} = \int_0^{\varphi_B} d\varphi N_{\gamma}(\theta_{\min}(\varphi)) \quad (5)$$

where φ_B is the length of the dipole magnet expressed in radians, φ is the emission location inside the dipole in radians. We assume a full height $h = 10$ mm for the proposed antechamber in the TESLA arcs. Integrating Eq. (5) one obtains $N_{\gamma, \text{mag}} = 0.24$ for the photons of all energies hitting the inside chamber per beam particle per bend [14]. Considering only the photons with energy $W > \hbar\omega_m = 4$ eV, the integration gives $N_{\gamma, \text{mag}} = 0.0235$. Finally, one may define the photon flux as the total number of photons emitted per second by the particle beam current I or $\mathfrak{S}_{\gamma} = N_{\gamma} I/e$. Thus, the average photon flux at the wall in a DR FODO cell per meter and per second is

$$\frac{d\mathfrak{S}_{\gamma}}{ds} = \frac{I N_{\gamma, \text{mag}}}{e L_{\text{cell}}} \quad (6)$$

where $L_{\text{cell}} = 15.2$ m is the TESLA FODO arc cell length. The average photon flux is given in Table 2. In the limit of no antechamber, we obtain

$$\lim_{h \rightarrow 0} N_{\gamma, \text{mag}} = N_{\gamma, \text{tot}} \quad (7)$$

Note that the average number of photons per beam particle per meter with no antechamber in the arc is $N_{\gamma, \text{tot}}/L_{\text{cell}} = 0.7$ ph/m.

TESLA DR Damping Wiggler

The beam sizes in the TESLA wiggler section are $\sigma_x = 93$ μm and $\sigma_y = 5$ μm . Since radiation from different

parts of the electron trajectory adds incoherently in a wiggler magnet, it is usual to consider that synchrotron radiation is similar to that produced by an individual bending magnet, but $2N_w$ times as intense due to repetitive electron bending over the length of a $2N_w$ -pole wiggler.

We assume that synchrotron radiation emitted off axis and with small cone aperture is soon intercepted by the antechambers, on both sides of the wiggler vacuum chamber. In our calculation, we will consider the angular photon flux \mathfrak{S}_{γ} emitted in the horizontal direction $\theta_y = 0$. The related frequency spectrum in the forward direction [16] is given by

$$\left. \frac{d^3 \mathfrak{S}_{\gamma}}{d\theta_x d\theta_y d\omega} \right|_{\theta_y=0} = 2N_w \frac{3\alpha}{4\pi^2} \gamma^2 \frac{1}{\omega} \frac{I}{e} H_2(y) \quad (8)$$

where we have considered the envelope of the peak spectral lines maxima

$$H_2(y) = y^2 K_{2/3}^2(y/2) \quad \text{and} \quad y = \varepsilon/\varepsilon_c = \omega/\omega_c. \quad (9)$$

To study effects related to the synchrotron radiation in particle accelerator as the electron cloud effect or photon gas desorption, one is interested in the generation of electrons at the wall by photons with sufficient energy. An important consideration is that in a wiggler, the opening radiation angle of emission depends on the energy of the emitted photons.

Most importantly, radiation is emitted at a fundamental angular wavelength λ_1 and its harmonics k . The correspondent angular frequency of the higher harmonics is given by

$$\omega_k = \frac{2\pi c}{\lambda_w} \frac{2\gamma^2 k}{1 + K^2/2 + \gamma^2(\theta_x^2 + \theta_y^2)} \quad (10)$$

where λ_w is the wiggler period and the dimensionless strength wiggler parameter $K = 93.4\lambda_w[\text{m}] B_0[\text{T}] = 59.7$. In the forward direction, $\theta_x = \theta_y = 0$, the corresponding photon energy is in practical units

$$\varepsilon_k[\text{eV}] = \hbar\omega_k = 9.4963 \frac{k (E[\text{GeV}])^2}{\lambda_w [\text{m}] (1 + K^2/2)}. \quad (11)$$

The spectral bandwidth and the polar opening angle decrease with the harmonic number as

$$\frac{\Delta\lambda}{\lambda} = \frac{1}{kN_w}, \quad \sigma_k \approx \frac{1}{\gamma} \sqrt{\frac{1 + K^2/2}{2kN_w}}. \quad (12)$$

In the TESLA wiggler, the 13th harmonic of the fundamental frequency ω_1 corresponds to a photon energy 4.3 eV,

$$\varepsilon_{k=13} (\text{eV}) = \hbar\omega_1 k|_{k=13} = 4.3 \text{ eV}, \quad \sigma_{k=13} = 34 \mu\text{m}. \quad (13)$$

Thus, only harmonics higher than the 13th correspond to photons with energy higher than 4 eV, needed for photoemission. An important consequence is that high energy photons within the emission cone are transmitted out of the wiggler. In fact, at the end of the wiggler section of

Table 2: Average photon flux in the TESLA arc hitting the vacuum chamber. The photon flux per meter per second, Eq. (6), at the chamber wall for different full height antechamber h . The percentages are intended with respect to the flux of photons of all energies and a vacuum chamber with “no antechamber”.

	no antechamber	$h = 6$ mm	$h = 8$ mm	$h = 10$ mm
Photons of all energies	7.1×10^{17} ph/s/m	4.6%	3.1%	2.2%
Photon of energy $W > 4$ eV	88%	0.75%	0.34%	0.2%

length L_w the emission cone dimensions are smaller than the wiggler beam pipe vertical semi-axis

$$L_w \sigma_{k=13} = 8.4 \text{ mm} < b = 9 \text{ mm}. \quad (14)$$

the photons within the emission cone are transmitted through the wiggler final aperture and are not able to hit the wiggler chamber walls. Higher harmonics have even smaller opening angles.

The number of photons emitted in the forward cone represents $\approx 90\%$ of the total photon flux and it is obtained integrating the frequency spectrum Eq. (8)

$$\int_{\omega_1}^{\infty} d\omega \frac{d^3 \mathfrak{S}_\gamma}{d\theta_x d\theta_y d\omega} = 4.4 \times 10^{17} \text{ ph/s} \quad (15)$$

where we have assumed that the radiation is emitted in a cone¹ $\sigma_{k=13}^2$. The photons emitted at larger angles $\approx 10\%$, will be able to hit the chamber wall. Then, the average number of photons per beam particle hitting the wiggler chamber wall is

$$1.4 \times 10^8 \text{ ph/m} \quad \text{or} \quad 2.5 \times 10^{10} \text{ photoelectrons/m}^3$$

where to estimate the photoelectrons we have assumed a constant photoelectron yield $Y = 0.1$ and vacuum chamber parameters listed in Table 1.

GLC/NLC DR Damping Wiggler

The GLC/NLC DR arc vacuum chambers are provided with an antechamber design. Following similar arguments, the number of photons emitted per NLC magnet is given by Eq. (1) $N_{\gamma,\text{tot}} = 8.1$. Integrating the right-hand-side of Eq. (5) one obtains $N_{\gamma,\text{mag}} = 0.11$ and 0.023 , respectively, for photons of all energies and photons with energy $W > 4$ eV. Thus only 1.3% of photons of all energies hit the vacuum chamber while only 0.26% of the photons emitted hit the chamber with $W > 4$ eV needed for photoemission.

SIMULATION RESULTS OF THE CLOUD GENERATION AND DEVELOPMENT

Simulation results for the electron cloud in the wigglers and arc regions of the NL/GLC X-Band positron main damping ring have been reported previously in [19]. In the

¹In the literature, the photon flux is usually expressed in units of mrad^{-2} emission angle, in which case the flux is 3.2×10^{20} ph/s/mrad².

present paper, we also report about recent simulation results for the TESLA DR design. In particular, for the analysis of the electron dynamics in a wiggler, we have used a cylindrical mode representation of the magnetic field [20]

$$\begin{aligned} B_\rho &= \sum c_{mn} I'_m(nk_z \rho) \sin(m\phi) \cos(nk_z z) \\ B_\phi &= \sum c_{mn} \frac{m}{nk_z \rho} I_m(nk_z \rho) \cos(m\phi) \cos(nk_z z) \\ B_z &= -\sum c_{mn} I_m(nk_z \rho) \sin(m\phi) \sin(nk_z z) \end{aligned} \quad (16)$$

where I_m are the modified Bessel function of order m , c_{mn} are the coefficients of the cylindrical expansion, and the wiggler field is represented in our simulations by the first 10 and 60 modes, respectively, in the case of the NLC and TESLA DR wigglers. The wiggler field used in our simulation code POSINST is shown in Figs. 5 and 6. A rectangular vacuum chamber profile with antechamber on both sides is included in the simulations.

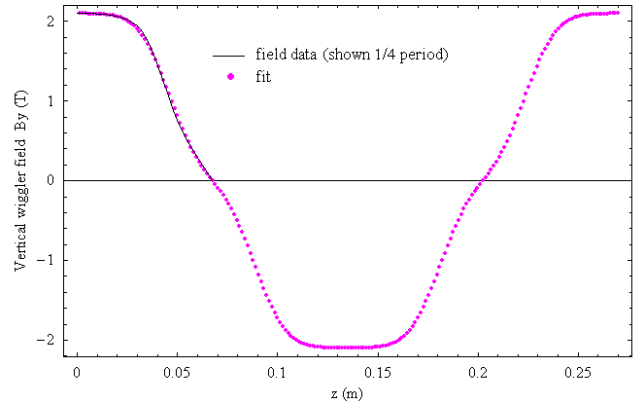


Figure 5: Vertical wiggler magnetic field model for the NLC DR, compared with the field data (shown 1/4 period). Magnetic field at gap center is 2.1 T and the wiggler period is $\lambda_w = 0.27$ m.

The most stringent requirements are in the wiggler sections of either the X-Band or the TESLA damping rings, where simulations indicate that δ_{max} must be below $\sim 1.2 \div 1.25$ to avoid the electron cloud as illustrated in Fig. 7 and in Table 3. Snapshots of the bi- and tri-dimensional electron cloud distributions are shown in Fig. 8 and Fig. 9 respectively. These simulation results have been obtained assuming a two-dimensional electron cloud space charge electric field, averaged over the length of the simulated section. The exact electron dynamics in a wiggler would re-

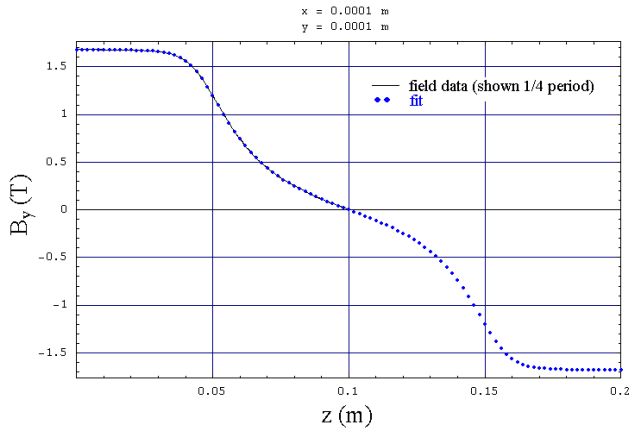


Figure 6: Vertical wiggler magnetic field simulation model fit for the TESLA DR, compared with the field data (shown 1/4 period). Magnetic field at gap center is 1.6 T and the wiggler period is $\lambda_w=0.40$ m.

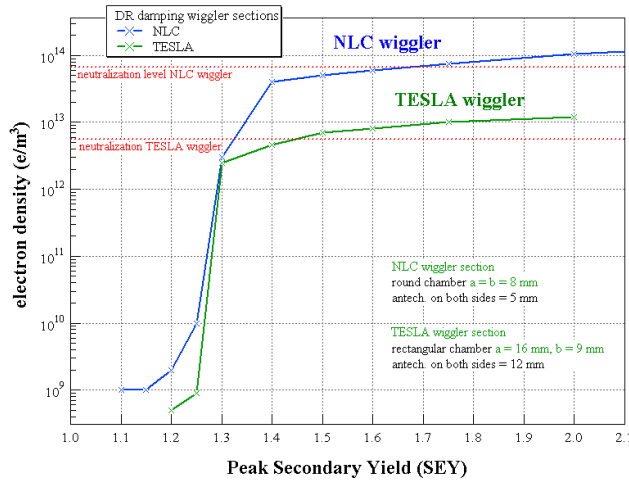


Figure 7: Simulation of electron cloud as a function of secondary electron yield in GLC/NLC and TESLA DR wigglers. Photoelectrons are not included in this simulation.

quire a 3D space charge electric field, not yet implemented in the code.

There are also concerns for the arc sections of both linear collider damping ring designs. The arcs of the TESLA DR do not include an antechamber. In this case, the synchrotron radiation generates a large quantity of photoelectrons and an electron cloud is always present independent of the SEY, as shown in Fig. 10. In particular, in the TESLA DR arc dipoles and quadrupoles without an antechamber design, a photo-electron cloud is present even for δ_{\max} as low as 1.1. Based on the electron cloud simulation results, an antechamber design for the TESLA DR arcs vacuum chamber is recommended.

An antechamber design with full height $h = 10$ mm, for the TESLA arc chambers has been considered in the simulations. Results show that an electron cloud develops in a dipole section for $\delta_{\max} \sim 1.3$. Note that in our SEY model,

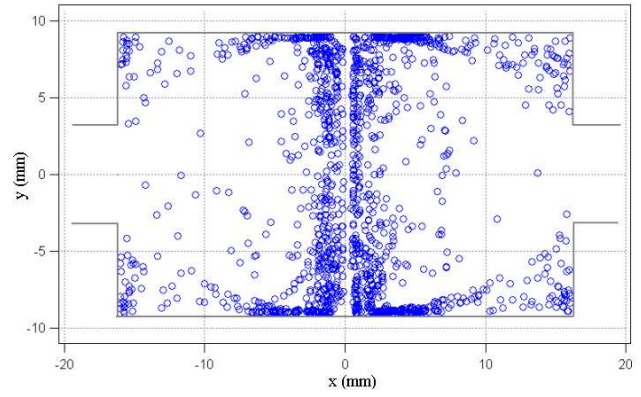


Figure 8: Snapshot of the $x - y$ phase space distribution in a TESLA DR wiggler.

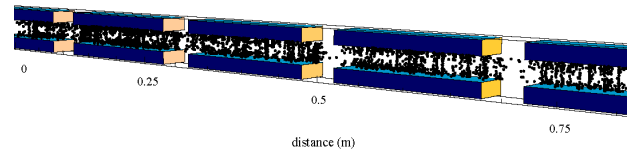


Figure 9: Snapshot of the $x - y - z$ tri-dimensional electron distribution in a TESLA DR wiggler.

the energy value E_{\max} at which the SEY is maximum is assumed to vary with δ_{\max} [18]. The electrons in a dipole typically concentrate in vertical stripes. Simulation results for a TESLA arc dipole section are shown in Fig. 11. The typical stripe distribution may be explained as follow. The electrons are constrained to move along the dipole vertical field lines. The electron energy gain depends on its horizontal position with respect to the bunch axis. The horizontal location at which the energy kick results in the maximum multiplication, or peak SEY, should correspond to the location of the stripes. Typically in a dipole, one single stripe is present for low beam intensity and two stripes are present for high beam intensity.

In the X-band damping ring, the arc vacuum chamber is provided with an antechamber. In a dipole section, $\delta_{\max} < 1.3 \div 1.4$ is required to prevent the formation of an electron cloud.

In the field free regions of the TESLA DR long straight sections, the large vacuum chamber radius 50 mm and bunch spacing 20 ns set the threshold conditions for electron multiplication at $\delta_{\max} \sim 2.0$ [19], which represents a safe margin. Due to the short bunch spacing and smaller vacuum chamber sizes of the X-Band DR the threshold for the electron cloud in field free regions is lower at $\delta_{\max} = 1.5$.

Simulations confirm the electron trapping mechanism in quadrupoles. The electron cloud decay time is very long due to the trapping of electrons in the quadrupole magnetic field. Note that the beta functions are generally high in quadrupoles and the electron cloud may have a greater effect on the beam stability in those regions. More estimates

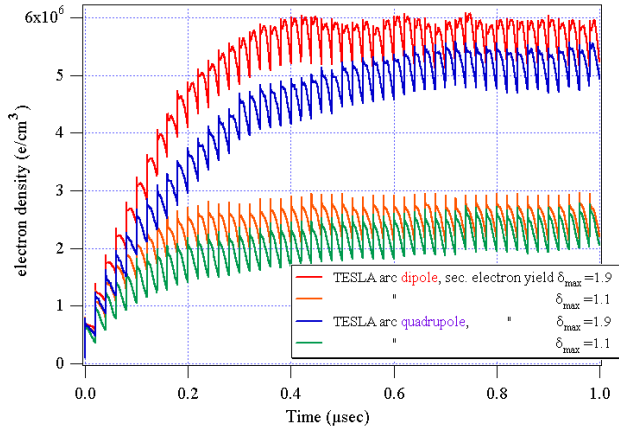


Figure 10: Simulation of the electron cloud effect in the TESLA DR arc dipoles and quadrupoles without antechamber. A (photo)electron cloud is present even for δ_{\max} as low as 1.1.

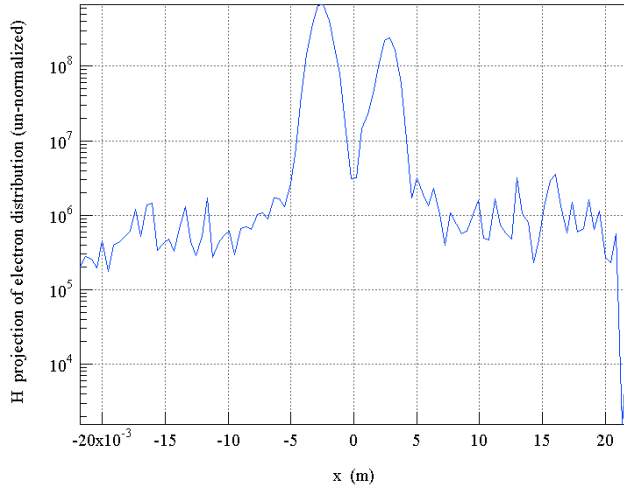


Figure 11: Horizontal projection of the particle distribution (unnormalized) in a TESLA DR arc dipole with an antechamber design. Assuming $\delta_{\max} = 1.3$ and $E_{\max} = 180$ eV.

are needed.

Secondary yield thresholds for the development of the electron cloud in both linear collider DR design are listed in Table 3.

SINGLE-BUNCH INSTABILITY

The results for the single-bunch fast head-tail instability in the X-band and TESLA damping rings have been obtained with the HEAD-TAIL simulation code developed by G. Rumolo and F. Zimmermann at CERN [8] and benchmarked against two other different simulation codes, QUICKPIC [10] and PEHTS [11]. Since the synchrotron tune is small, the number of cloud-beam interactions per turn has been typically varied between 1 and 30. A discrete Fast Fourier Transform (FFT) in two dimensional space

and a particle-in-cell (PIC) algorithm are used to compute the electron cloud and beam potentials. The electrons oscillate in the linearized beam potential with an angular frequency $\omega_{c,y}$ given by

$$\omega_{c,y}^2 = \frac{2\lambda_b r_e c^2}{(\sigma_x + \sigma_y)\sigma_y} \quad (17)$$

where λ_b is the beam line density and $\sigma_{x,y}$ the transverse beam size.

Due to the electron cloud oscillation and pinching, the cloud density increases along the bunch. An electron cloud wakefield is established which drives the oscillations of the tail of the bunch. The interchange of the head with the tail by synchrotron oscillations is a damping mechanism for the fast head-tail effect. Thus, the maximum allowed electron cloud density depends on the synchrotron tune and the driving force. Also, note that the head-tail effect depends on the average electron cloud density $\bar{\rho}_{el}$ along the ring, given by

$$\bar{\rho}_{el} = \frac{1}{C} \oint ds \rho_{el}(s) \quad (18)$$

In the X-band MDR, an head-tail instability is observed to occur for an average electron cloud density close to 2.0×10^{12} e/m³, as shown in Fig. 12, with growth time on the order of 100 μ s. The three codes show consistent results. This is one order-of-magnitude lower than the expected cloud neutralization level if a cloud is allowed to form as shown in Table 4. A slightly positive chromaticity or a larger synchrotron tune increase the instability threshold as expected, but this is unlikely to provide the margin of safety that is desired. In the TESLA DR the electron cloud

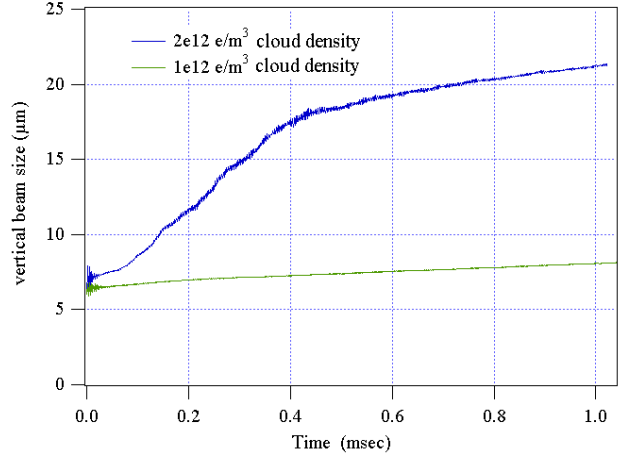


Figure 12: Simulation of single-bunch beam instability from electron cloud in GLC/NLC Damping Ring field free region.

is expected to develop in the arcs and wiggler sections. To take into account the electron distribution in dipole and wigglers, we have used two different initial electron distributions as input for HEAD-TAIL simulation code.

First, we have used an initially uniform electron density distribution and the threshold of the instability develops

Table 3: Secondary electron yield (δ_{\max}) thresholds and neutralization electron cloud density for the development of an electron cloud in the TESLA and GLC/NLC linear collider damping rings.

Damping Ring location	δ_{\max} threshold	neutr. cloud density (e/m^3)
GLC/NLC field free region	$1.5 \div 1.6$	2×10^{13}
” arc dipole	$1.3 \div 1.4$	2×10^{13}
” arc quadrupole	$1.2 \div 1.25$	2×10^{13}
” damping wiggler	$1.2 \div 1.3$	6×10^{13}
TESLA long straight sections	$2.0 \div 2.1$	4×10^{11}
” arc dipole without antech.	photoe ⁻ dominated	2×10^{12}
” arc dipole with antechamber	1.3	2×10^{12}
” arc quadrupole without antech.	photoe ⁻ dominated	2×10^{12}
” arc quadrupole with antech.	-	2×10^{12}
” damping wiggler	$1.2 \div 1.3$	5×10^{12}

for an average cloud density over the ring is $\sim 2 \times 10^{11}$ e/m^3 , as shown in Fig. 13. The instability threshold for the 17000 m long TESLA DR is below the expected cloud neutralization level. TESLA DR simulation results have been benchmarked against the three codes and are consistent, see Fig. 13, 15, 16. Furthermore, the instability is accompanied by severe beam particle losses in the first few turns, as shown in Fig. 14.

One may estimate the head-tail effect from the TESLA wiggler sections only. Since the integrated electron cloud density is of importance, the instability threshold can be estimated by scaling the length of the DR to the length of the 500 m long wiggler sections. According to Eq. (18), an average cloud density (17000 m)/(500 m) \approx 30 times higher or $3-6 \times 10^{12}$ e/m^3 should be expected to cause an instability, which is in agreement with simulations [21].

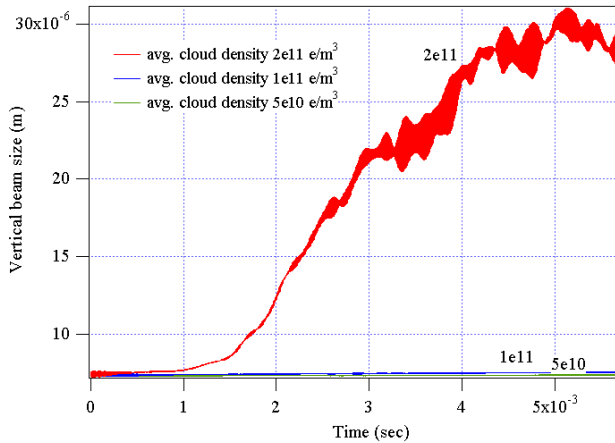


Figure 13: Simulated vertical beam size increase in time assuming different cloud density, HEAD-TAIL code. The head-tail instability develops for an average cloud density of $1-2 \times 10^{11}$ e/m^3 . An initially-uniform electron cloud distribution is assumed. The length of the run is 100 turns.

As a second approach, we have also used an initial electron cloud distribution with vertical stripes, typical of

dipole or wiggler sections. HEAD-TAIL allows to set rectangular vertical stripes, see an example in Fig. 17. The cloud density is 10 times higher in the two stripes regions. In the TESLA wiggler, vertical stripes in the electron distribution start to be visible at nominal beam conditions, as shown in Fig. 8. Similarly, stripes occur for a TESLA arc dipole section as previously shown Fig. 11. To simulate the stripes electron distribution in a wiggler section, we set two rectangular stripes at distances $a = \pm 0.7$ mm and width ~ 300 μ m. A single-bunch instability is expected for a cloud density $1 \div 3 \times 10^{10}$ e/m^3 . The results of the HEAD-TAIL simulation are shown in Fig. 18.

Thus, the simulations of the single bunch instability depend sensibly on the initial cloud distribution and the results may vary by \sim an order of magnitude.

Finally, we have used CLOUD-MAD to estimate the incoherent tune shift due to the bunch passing through the TESLA wiggler. Assuming an equilibrium electron density of 6×10^{12} e/m^3 a large vertical tune spread of 0.3 is computed, as shown in Fig. 19.

A summary of the electron cloud instability thresholds for both damping rings are listed in Table 4.

Coupled-bunch instability

The coupled bunch instability has been estimated with the code POSINST. In the simulations, after reaching an equilibrium cloud density a bunch is displaced by a defined amount and the wake acting on the subsequent bunches is computed [7]. Considering the ring filled with M equally-spaced bunches, each with a particle population N_p , we compute the coherent dipole frequency Ω_μ corresponding to the dipole oscillation mode μ by

$$\Omega_\mu - \omega_\beta = \frac{ce^2 N_p}{4\pi E \nu_\beta} \sum_{k=0}^{nw} W(k s_B) e^{2\pi i k (\mu + \nu_\beta) / M} \quad (19)$$

where $\omega_\beta = \omega_0 \nu_\beta$ is the betatron angular frequency, ν_β is the horizontal or vertical tune, the collective mode oscillation number is given by $\mu = 0, 1, 2, \dots, M - 1$, E is

Table 4: Threshold value of the electron cloud density, in units of e/m^3 , for an incoherent tune spread limit $\Delta\nu = 0.05$, and for the onset of single- and coupled-bunch instability. The density at average beam neutralization level is also shown.

Parameter	X-Band MDR	TESLA DR
Incoherent tune spread $\Delta\nu = 0.05$	1.6×10^{12}	2.3×10^{10}
Single-Bunch instability	2.0×10^{12}	$1 \div 3 \times 10^{10}$
Coupled-Bunch instability	3.0×10^{13}	1.6×10^{13}
Av. neutralization	2.5×10^{13}	8.0×10^{11}

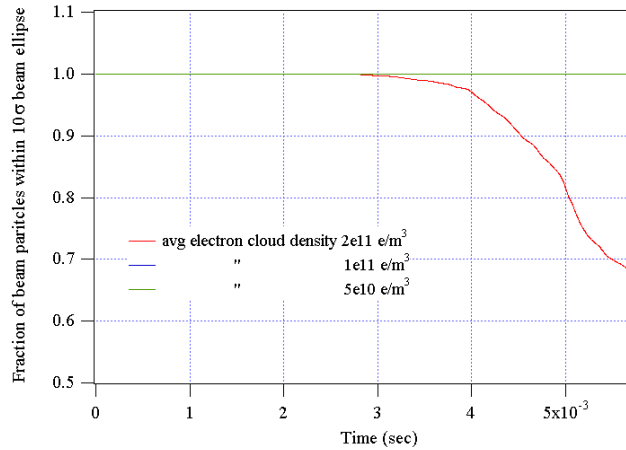


Figure 14: Beam losses following single-bunch instability. Beam particles within the $10\text{-}\sigma$ beam ellipse. An initially uniform electron cloud distribution is assumed. Beam losses occurs at $2 \times 10^{11} e/m^3$. The length of the run is 100 turns.

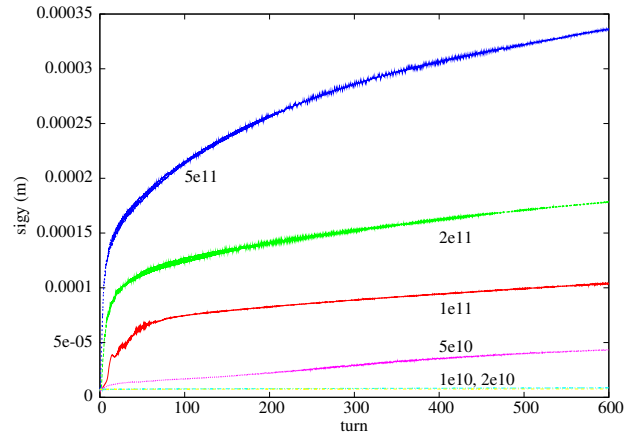


Figure 16: Simulation of single-bunch beam instability from electron cloud in the TESLA Damping Ring using PEHTS code assuming an initially uniform electron cloud distribution.

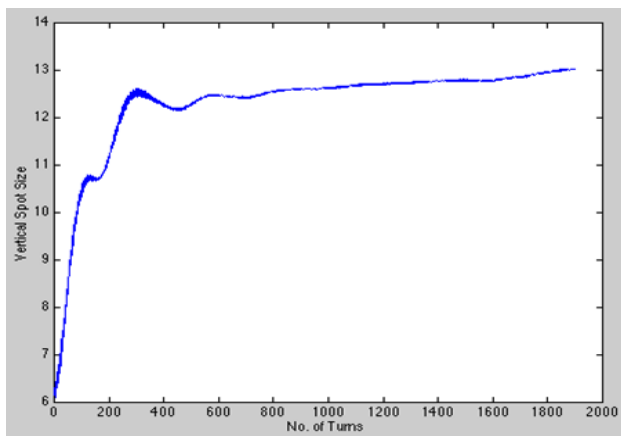


Figure 15: Simulation of single-bunch beam instability from electron cloud in the TESLA Damping Ring using QUICKPIC code for an initially uniform electron cloud distribution [22].

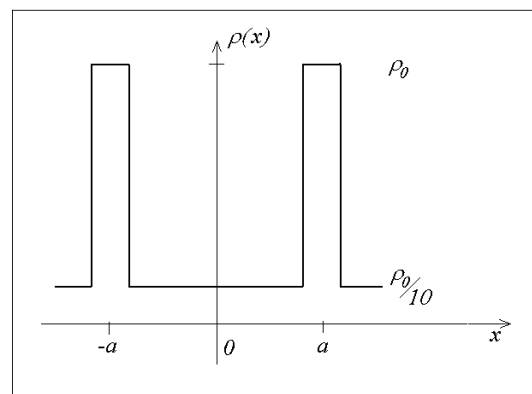


Figure 17: Schematic of the horizontal projection of the particle distribution assumed in the HEAD-TAIL code to resemble a wiggler, or two-stripes dipole like, electron distribution. The electron distribution is approximated rectangular and the cloud density is an order of magnitude higher inside the stripe regions.

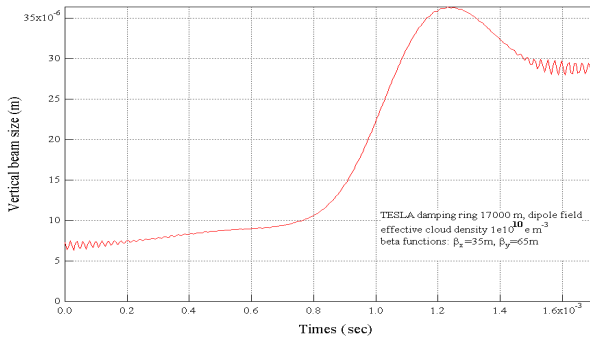


Figure 18: Simulation of single-bunch beam instability from electron cloud in the TESLA Damping Ring using the HEAD-TAIL code, assuming an horizontal electron cloud distribution with stripes.

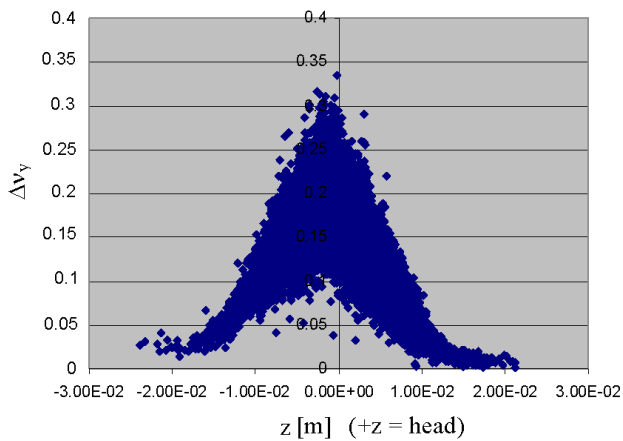


Figure 19: Vertical tune shift after passing through the TESLA wiggler beam line which has 432 meters of wiggler in 520 meters of beam line. An electron cloud density of $6 \times 10^{12} \text{ e/m}^3$ is assumed. The magnetic field is not included.

the beam energy, and the summation is extended to the nw first subsequent bunches, here $nw=10$. The threshold for a coupled-bunch instability in the X-band main damping ring is at a cloud density $> 3.0 \times 10^{13} \text{ e/m}^3$, see Fig. 20, and in the TESLA damping ring is at cloud density $> 1.6 \times 10^{13} \text{ e/m}^3$. The estimated growth time for these threshold density levels is $100 \mu\text{s}$, which can be corrected by feedback.

LINEAR COLLIDERS LOW EMITTANCE TRANSPORT LINES

Single bunch effects

Using the code CLOUD_MAD, in the positron transport lines of the NLC linear collider bunch compressor, the main linac, and the beam delivery system we estimate thresholds for emittance increase or beam size blow-up ranging from $1.0 \times 10^{11} \text{ e/m}^3$ to $5.0 \times 10^{13} \text{ e/m}^3$ [23, 24]. Simu-

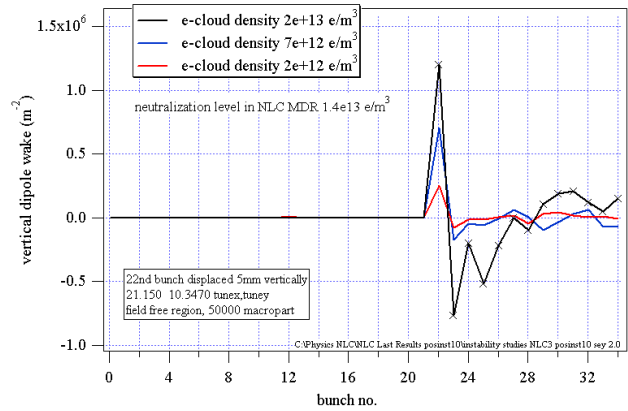


Figure 20: Long Range wake field in the NLC DR.

lation of beam-size blow-up at the IP as a function of the cloud density in the beam delivery system are shown in Fig. 21. In the main linac and the bunch compressor prelinac, the electron cloud may cause a modulation of the position within a single bunch, while in the arcs of the bunch compressor or the BDS, it causes a mismatch of the optical functions. Again, these thresholds are below the neutralization levels however, as will be discussed, the cloud does not necessarily reach neutralization along the short bunch train and fully dissipates between machine pulses. In the positron transport lines, electron cloud generation is only expected to be an issue for the normal conducting X-band linear colliders where the bunches are closely spaced, and not for TESLA where the bunch spacing is 337 ns (176 ns at 800 GeV c.m.), see Fig. 22.

In the X-Band collider design, the bunch train is roughly 268 ns in length. Depending on the vacuum chamber radius, material and conditioning, an electron cloud can be generated which will approach the neutralization density. For example, with a 10 mm radius chamber and a secondary electron yield of 2, the electron cloud reaches a density of roughly $1 \times 10^{14} \text{ e/m}^3$ by the end of a positron bunch train, as shown in Fig. 23. The electron cloud density just after the passage of a 268 ns bunch train is a strong function of the vacuum chamber radius as well as the SEY. By decreasing δ_{max} to 1.5 or increasing slightly the vacuum chamber radius, as shown in Fig. 24, the peak cloud density can be reduced to acceptably low values. However, the effects of photoelectrons, computed in [14], must still be taken into account in both normal- and super-conducting linear colliders.

Coupled-bunch instabilities have been estimated analytically for the NLC BDS and the threshold is expected to be at $3.6 \times 10^{12} \text{ e/m}^3$.

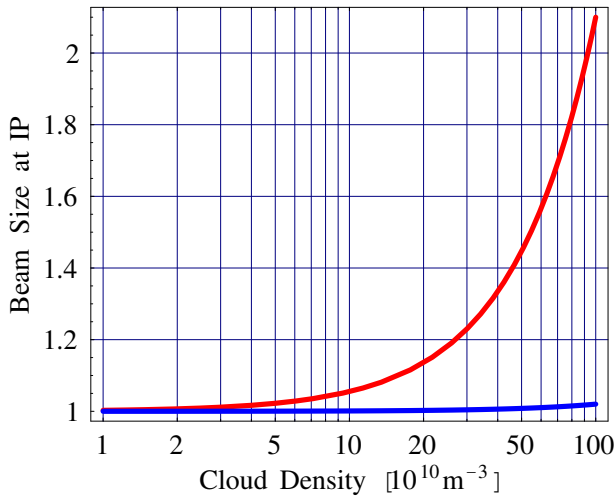


Figure 21: Simulation of vertical beam size blow-up at the IP as a function of the cloud density in the beam delivery system, using CLOUD_MAD code.

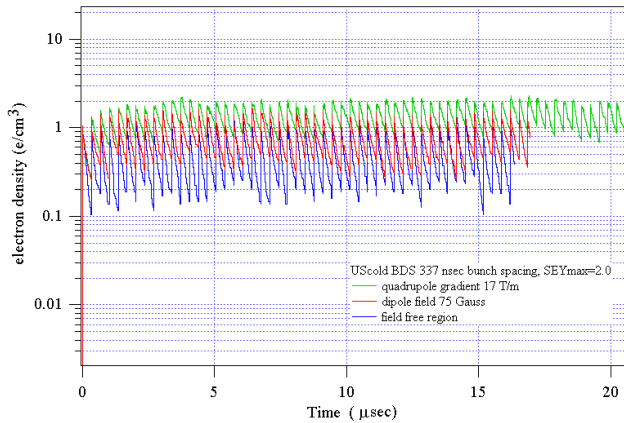


Figure 22: Simulated electron cloud density, in units of e/cm^3 , in the TESLA and USCold BDS, from ionization of residual gases. Assumed $\delta_{max} = 2.0$.

R&D EFFORT TO REDUCE THE SEY

Conditioning and Recontamination Under Vacuum

SLAC has an active R&D effort to find a cure for the electron cloud effect by surface treatments. In particular, we are measuring the SEY of thin film coatings, exploring durability and conditioning strategies, investigating a new surface profile design and finally planning to install test demonstration chambers in PEP-II. The value of δ_{max} , typically ~ 3.0 for as-received aluminum 6063 vacuum chamber material, is unacceptably high for either damping ring design. Various possible remedies to decrease the SEY are being evaluated. Thin film coatings reduce the SEY, but not enough. The specified SEY values have been reached for a TiN or TiZrV coated surface after conditioning by surface electron bombardment as shown in Fig. 25

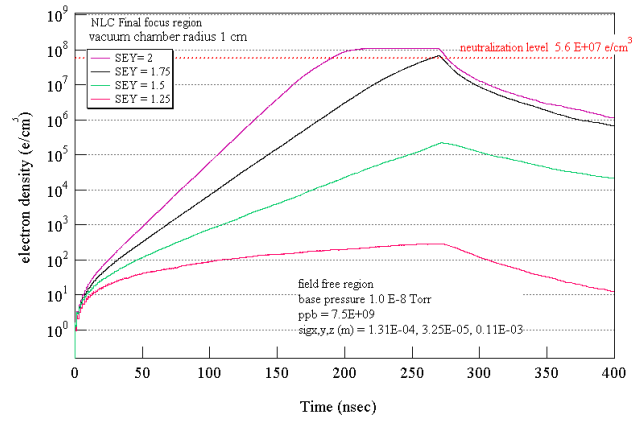


Figure 23: Simulated electron cloud build-up by residual gas ionization, in units of e/cm^3 , in the X-Band BDS for different values of δ_{max} , during the pass of a bunch train.

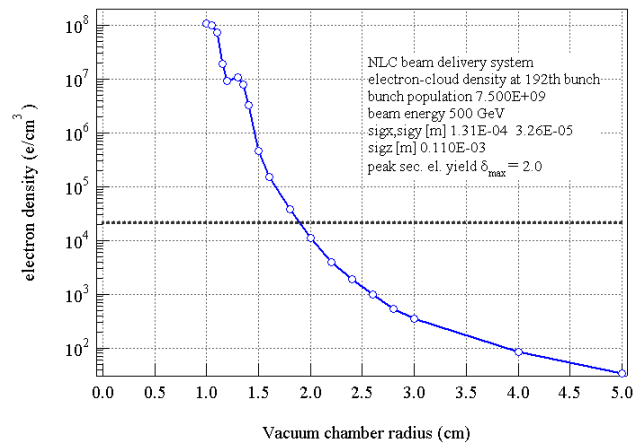


Figure 24: Cloud density just after the pass of a bunch train, in units of e/cm^3 , as a function of vacuum chamber radius, in the X-Band BDS. The source is residual gas ionization.

[25]. Nevertheless, to keep the SEY at very low values and in a stable way under the effect of gas recontamination is a challenging task. Recontamination of the surface under vacuum tends to re-increase the SEY as shown in Fig. 26.

In accelerator environments there is a limitation to the lowest reachable SEY. As the SEY decreases on the surface due to the electron bombardment, the electron cloud tends to disappear. The electron conditioning mechanism will eventually stop when the cloud is dissipated and may never reach the lowest values shown in Fig. 25. Remarkable *in situ* measurements in the SPS at CERN, show that δ_{max} does not decrease lower than ~ 1.6 in dedicated runs with LHC-type beams [26]. Simulations show that in the X-band damping ring, the electron wall current on the beam pipe from the electron cloud itself is large, and the required electron conditioning dose can be achieved in a few tens of hours of beam operation. Concerns have also been expressed about the coating durability under beam operations and the effective conditioning time which may be longer in an accelerator environment. For these reasons, we are

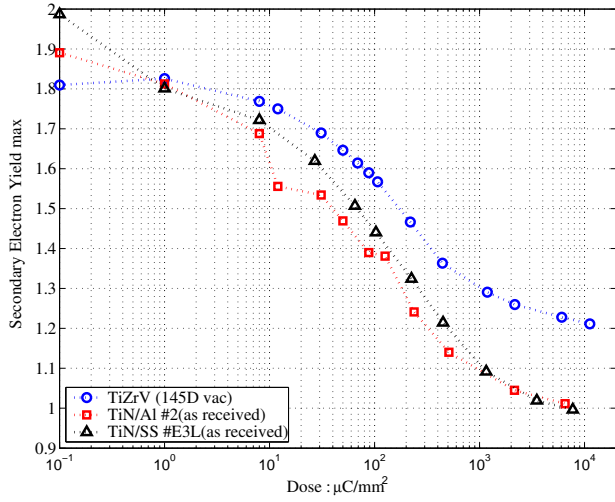


Figure 25: Measurements of effect of electron conditioning on TiN and TiZrV coatings.

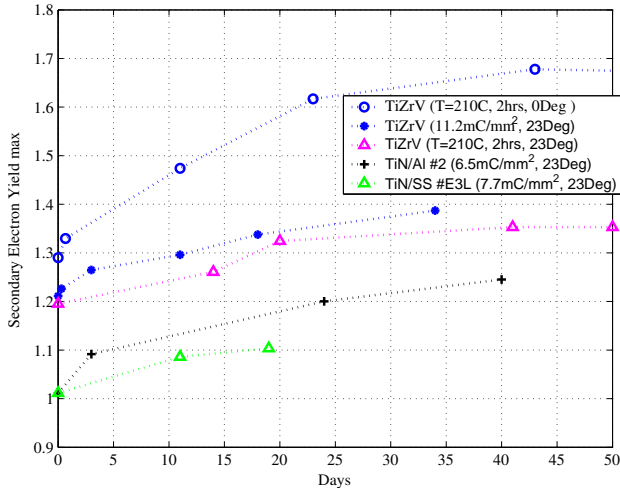


Figure 26: Recontamination under vacuum. Laboratory measurements of samples maintained under high vacuum.

planning to install samples in PEP-II to monitor surface coatings and measure the SEY as a function of beam time.

Drastic Reduction of the SEY: Groove Surface Profile

We are also developing a metal surface with a new specially designed grooved profile [27, 28]. Such a surface is being fabricated and is expected to reduce the escape probability of secondary emitted electrons, reducing considerably the effective SEY. Simulations estimates show a reduction of the secondary yield by a factor of 2. In the simulations we have used a model described in [17] where the energy spectrum is defined as a sum of the independent electron elastically reflected, rediffused and true secondary

components

$$\frac{d\delta}{dE} = f_{1,e} + f_{1,r} + \frac{d\delta_{ts}}{dE} \quad (20)$$

where

$$\frac{d\delta_{ts}}{dE} = \sum_{n=1}^{\infty} \frac{n P_{n,ts}(E_0) (E/\epsilon_n)^{p_n-1} e^{-E/\epsilon_n}}{\epsilon_n \Gamma(p_n) P(n p_n, E_0/\epsilon_n)} \times P((n-1)p_n, (E_0-E)/\epsilon_n) \quad (21)$$

The triangular grooves resulted in a good reduction in the secondary electron yield of 35%. Very promising results come from the rectangular groove concept as shown in Fig. 27, 28 where the reduction is ~50% and the effective SEY is < 0.8. The SEY of a second sample with scaled dimension to obtain a 5 mm groove depth is shown in Fig. 29, where the measured δ_{max} is as low as 0.6.

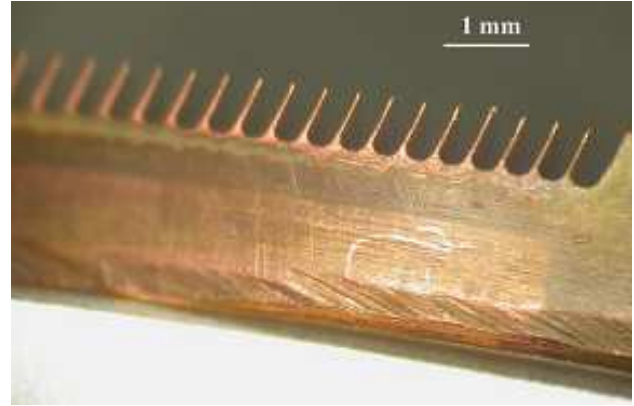


Figure 27: Copper groove sample with 1 mm depth and 0.3 mm step between grooves.

Following the highly promising results, we are planning to install a 6 m long section to test the groove concept with dedicated chambers equipped with proper electron diagnostics [29] in the PEP-II accelerator.

Other techniques such as ion conditioning are also under study. Solenoid windings have proven very effective in reducing the cloud density in existing accelerator machines. This solution can be applied in the beam delivery and bunch compressor system and in the magnetic free regions of a damping ring. Furthermore, simulations show that increasing the chamber aperture is beneficial in reducing the cloud density in the Low Emittance Transport sections. Because the electron cloud is an issue for many different facilities, there is a broad international effort on simulations, beam measurements and mitigation strategies. SLAC, LBNL and KEK are collaborating with USC, CERN and DESY on single-bunch simulation studies, with LBNL and BNL to produce TiZrV and TiN coated materials, with LANL to measure the electron cloud effect in quadrupoles and with CERN to measure electron cloud features in the SPS accelerator during dedicated LHC development studies.

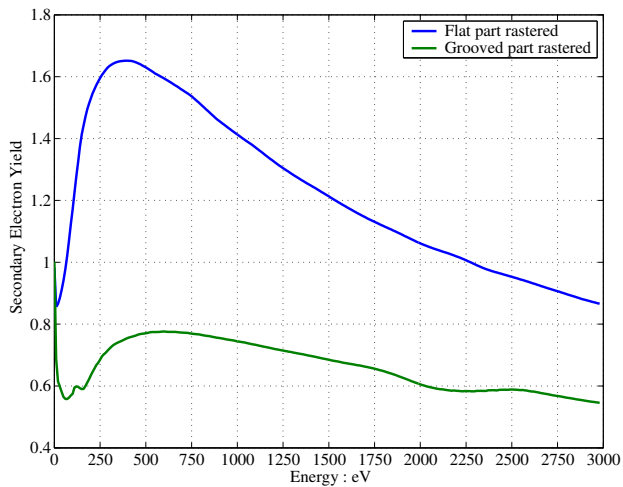


Figure 28: Copper sample with rectangular grooves. The upper curve represent the SEY of a flat part of the sample while the lower part is the SEY of the rectangular groove area. The groove parameters are ~ 1 mm depth and 0.3 mm step between grooves.

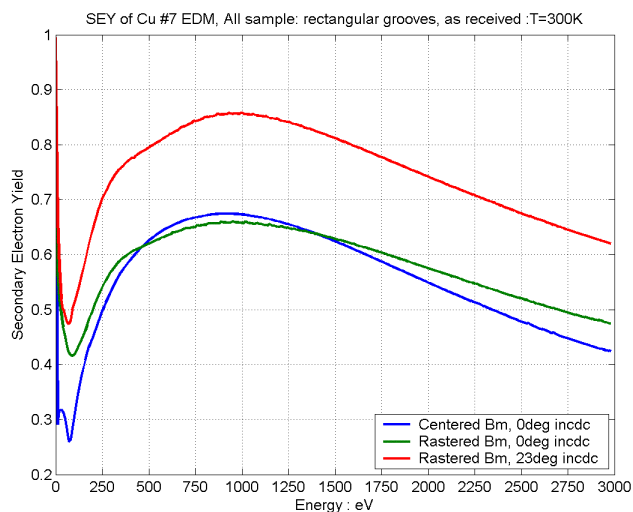


Figure 29: Copper sample with rectangular grooves. All the SEY curves are measured in the rectangular groove area. The upper curve refer to primary electron grazing at a 23° angle with respect to the groove profile. The groove parameters for this sample are: ~ 5 mm depth, 0.2 mm groove width, and 2 mm step between grooves.

ACKNOWLEDGMENTS

I would like particularly to thank M. A. Furman, G. Rumolo T. O. Raubenheimer, for their support in the simulations and very stimulating discussions, R. Kirby and F. Le Pimpec for measurements and many useful discussions. For contributions and useful discussions K. Ohmi and A. Ghalam, F. Zimmermann, E. Benedetto, A. Seryi, G. Stupakov. R. Wanzenberg, D. Shulte, S. Guiducci, K. Harkay, U. Irizo, M. Jiménez, J.M. Laurent, R. Macek, J. Seeman, C. Vaccarezza and A. Wolski. I am grateful to NERSC for

supercomputer support.

REFERENCES

- [1] M. Pivi and K. Ohmi, "Overview of the Electron Cloud Effect in the Linear Colliders," to be submitted to Phys. Rev. STAB.
- [2] For an updated summary and links on electron cloud studies, see E-CLOUD02: <http://slap.cern.ch/collective/ecloud02/>. See also the E-CLOUD04 workshop held on April 19-23, 2004: <http://icfa-ecloud04.web.cern.ch/icfa-ecloud04/>.
- [3] ILC-TRC Report 2003: [http://www.slac.stanford.edu/xorg/ilc-trc/2002/2002/repor t/03rep.htm](http://www.slac.stanford.edu/xorg/ilc-trc/2002/2002/repor%20t/03rep.htm).
- [4] A. Wolski and M. Woodley, "The NLC Main Damping Ring Lattice," NLC LCC-0113, LBNL CBP Tech Note-276, February 2003.
- [5] R. Brinkmann, K. Flöttmann, J. Roßbach, P. Schmüser, N. Walker, H. Weise, "TESLA Technical Design Report," March 2001.
- [6] M. Pivi, T. O. Raubenheimer and M. A. Furman, "Recent Electron Cloud Simulation Results for the NLC and for the TESLA Linear Colliders," in the Proceedings for PAC 2003, Portland, Oregon, US, May 12-16, 2003; also LCC-0124 Note http://www.project.slac.stanford.edu/lc/ilc/TechNotes/LCCNotes/lcc_notes_index.htm
- [7] M. A. Furman and G. R. Lambertson, "The Electron cloud Instability in the Arcs of the PEP-II Positron Ring," LBNL-41123/CBP Note-246, PEP-II AP Note AP 97.27, 1997. proc. Intl. Workshop on Multibunch Instabilities in Future Electron and Positron Accelerators (MBI-97), KEK, Tsukuba, Japan, 15-18 July 1997, KEK Proceedings 97-17, Dec. 1997 (Y. H. Chin, ed.), p.170.
- [8] F. Zimmermann and G. Rumolo, "Electron Cloud Simulation: Build Up and Related Effects," in Proceedings of the Mini-Workshop on Electron cloud Simulations for Proton and Positron Beams, CERN Geneva, 2002 [Yellow Report No. CERN-2002-001], p. 97.
- [9] CLOUD_MAD, T. Raubenheimer; reference page http://www-project.slac.stanford.edu/lc/local/AccelPhysics/Codes/Ion_MAD-Cloud_Mad/dbates/nlc_cloudmadtools.doc/cloud_mad/index.html
- [10] T. Katsouleas, A. Z. Ghalam, S. Lee, W. B. Mori, C. Huang, V. Decyk and C. Ren, "Plasma Modeling of Wakefield in Electron Clouds," CERN Geneva, 2002 [Yellow Report No. CERN-2002-001], p. 239.
- [11] K. Ohmi, "Particle-In-Cell Simulation of Beam-Electron Cloud Interactions," Proceedings of the Particle Accelerator Conference PAC2001, June 18-22, 2001, Chicago, IL, USA.
- [12] See TESLA contribution to ITRP Question and Answers from F. Zimmermann and R. Wanzenberg at <http://www.ligo.caltech.edu/~donna/ITRP-Questions%20and%20Matrix.htm>
- [13] R. Wanzenberg, F. Zimmermann, D. Shulte, in the proceedings of the E-CLOUD04 workshop.
- [14] M. Pivi, "Synchrotron Radiation in the Linear Colliders," to be published as ILC Tech. Note and NLC Tech. Note.

- [15] H. Wiedemann, *Particle Accelerator Physics II, Nonlinear and Higher-Order Beam Dynamics*, Springer-Verlag, 1993.
- [16] *X-Ray Data Booklet* Lawrence Berkeley Laboratory, Berkeley, CA, LBNL/PUB-490 Rev. 2, 2001.
- [17] M.A. Furman, M. Pivi Phys. Rev. STAB **5**, 124404, 2002.
- [18] N. Hilleret, V. Baglin, I.R. Collins, B. Henrist, G. Vorlauffer. CERN LHC Project Report 472, August 2001.
- [19] M. Pivi and T. Raubenheimer, "Recent Electron-Cloud Simulations Results for the Damping Ring of the NLC and TESLA Linear Colliders," in the Proc. of the PAC 2003 Conference, Portland, Oregon, US, 2003. See also: M. T. F. Pivi and T. Raubenheimer, "Electron Cloud effect in the Linear Colliders," ICFA NewsLetter no. 33, 2004.
- [20] M. Venturini, A. Wolski, A. Dragt in the Proc. of the PAC 2003 Conference, Portland, Oregon, US, 2003. Refer. RPAB023.
- [21] F. Zimmermann CERN, private communication June 2004.
- [22] A. Ghalam in the E-CLOUD04 workshop proceedings.
- [23] David Chen, Arthur Chang, Dan Bates, Mauro Pivi and Tor Raubenheimer, "Single Bunch Electron Cloud Effects in the LC Beam Delivery System," NLC LCC- 0126 Note, September 2003, http://www-project.slac.stanford.edu/lc/ilc/TechNotes/LCCNotes/lcc_notes_index.htm.
- [24] David Chen, Arthur Chang, Dan Bates, Mauro Pivi, "Single Bunch Electron Cloud Effects in the NLC Bunch Compressor System," NLC LCC-0131 Note, October 2003, see above link.
- [25] F. Le Pimpec, F. King, R. E. Kirby and M. Pivi, "Secondary Yield Measurements of TiN Coating and TiZrV Getter Film," LCC-128 Note (SLAC-TN-03-052), October 2003.
- [26] J. M. Jiménez, G. Arduini, P. Collier, G. Ferioli, B. Henrist, N. Hilleret, L. Jensen, K. Weiss, F. Zimmermann, CERN, LHC Project Report No. 632, April, 2003. Also <http://sl.web.cern.ch/SL/sli/Scrubbing-2002/NoelH.pdf>
- [27] A. Krasnov, "Molecular pumping properties of the LHC arc beam pipe and effective secondary electron emission from Cu surface with artificial roughness," CERN LHC Project Report 671.
- [28] G. Stupakov and M. Pivi, "Suppression of the effective SEY for a grooved metal surface," in the proceedings of the E-CLOUD04 workshop [2]. Electron conditioning results also to be published as LCC Note http://wwwproject.slac.stanford.edu/lc/ilc/TechNotes/LCCNotes/lcc_notes_index.htm.
- [29] R. A. Rosenberg, K. C. Harkay, "A rudimentary electron energy analyzer for accelerator diagnostics," Nuclear Instruments and Methods in Physics Research A **453** (2000), p.507-513.